RESEARCH ARTICLE | AUGUST 21 2025

Is there anybody out there? Ultrafast Rydberg–valence interactions in the photodissociation of trimethylamine

Derri J. Hughes ; Andrew W. Prentice ; Lauren Bertram ; Richard T. Chapman ; Luca Craciunescu ; Daniel A. Horke ; Peter Krüger ; Michael A. Parkes ; Henry J. Thompson ; Emma Springate ; James O. F. Thompson ; Yu Zhang ; Adam Kirrander ; Martin J. Paterson ; Russell S. Minns

J. Chem. Phys. 163, 074306 (2025)
https://doi.org/10.1063/5.0280626

The Journal of Chemical Physics ARTICLE pubs.aip.org/aip/jcp

Is there anybody out there? Ultrafast Rydberg–valence interactions in the photodissociation of trimethylamine

Cite as: J. Chem. Phys. 163, 074306 (2025); doi: 10.1063/5.0280626
Submitted: 13 May 2025 • Accepted: 24 July 2025 •
Published Online: 21 August 2025

Derri J. Hughes,[1] Andrew W. Prentice,[2] Lauren Bertram,[3] Richard T. Chapman,[4] Luca Craciunescu,[2] Daniel A. Horke,[5] Peter Krüger,[5] Michael A. Parkes,[6] Henry J. Thompson,[1] Emma Springate,[4] James O. F. Thompson,[4] Yu Zhang,[4] Adam Kirrander,[3] Martin J. Paterson,[2] and Russell S. Minns[1,a)]

AFFILIATIONS

[1] School of Chemistry and Chemical Engineering, University of Southampton, University Road, Highfield, Southampton SO17 1BJ, United Kingdom
[2] School of Engineering and Physical Sciences, Heriot-Watt University, Edinburgh EH14 4AS, United Kingdom
[3] Physical and Theoretical Chemistry Laboratory, Department of Chemistry, University of Oxford, South Parks Road, Oxford, United Kingdom
[4] Central Laser Facility, STFC Rutherford Appleton Laboratory, Didcot, Oxfordshire OX11 0QX, United Kingdom
[5] Institute for Molecules and Materials, Radboud University, Heijendaalseweg 135, 6525 AJ Nijmegen, The Netherlands
[6] Department of Chemistry, University College London, 20 Gordon Street, London WC1H 0AJ, United Kingdom

[a)] **Author to whom correspondence should be addressed:** R.S.Minns@soton.ac.uk

ABSTRACT

Trimethylamine (TMA) is a tertiary aliphatic amine that stands as a potential marker for life beyond Earth due to only being naturally produced *via* biotic means. However, its propensity to undergo photodissociation in the gas phase when excited by a deep ultraviolet photon means that its amine daughter product could serve as an additional biomarker and confirmational spectral signature of TMA in exoplanetary atmospheres. The photochemistry of TMA is dominated by strong Rydberg–valence state interactions. To understand how these interactions lead to its amine photoproduct, we employ time-resolved extreme ultraviolet photoelectron spectroscopy where TMA is pumped by a 200 nm femtosecond laser pulse and analyze the results with the help of electronic structure calculations of the excited state potential energy surface relevant to the process. Our combined experimental and theoretical study indicates that from the decay of the initially prepared $3p_z$ state (time-constant 400 fs), internal conversion through the remaining 3p manifold (4.4 ps) and the 3s state (67 ps) states competes with ultrafast photodissociation, forming ground state dimethyl amidogen (DMA) and CH_3 ($\nu_2 = 4$) radical products. Decay of the 3s state reveals the formation of a second product pair, forming DMA in a low-lying excited state, DMA ($\tilde{A}^2A_1$), and vibrationally cold CH_3. We suggest that the rapid dissociation channel arises from a near-planar geometry accessed in the $3p_z$ state and the longer time channel arises from the excited state population, accessing a pyramidal geometry in the 3s state.

I. INTRODUCTION

The question of *"are we alone in the universe?"* has long been at the heart of astrophysical research. Although an interdisciplinary problem, the chemical approach has been to use observational spectroscopy to seek out biomarkers—molecules that are produced or regulated by living organisms and, thus, indicate their presence in any of its forms.[1–4] The molecules O_2, O_3, CH_3Cl, N_2O, and CH_3SCH_3 are all traditionally used as biomarkers[5–8] to which the former two are indicative of photosynthetic life and the latter are indicative of microbial life. However, the main challenge faced by their use is that they all have biotic and abiotic (atmospheric, photochemical, volcanic) synthetic origins; thus, they do not reliably indicate the presence of extraterrestrial life.[9] Therefore, more reliable and specific biomarkers are paramount to the ongoing search.

The use of complex organic molecules may be an obvious solution; however, they must be known only to be produced naturally through biotic schemes, as this would provide a definitive indication of the presence of extraterrestrial life.[10–13] Trimethylamine (TMA) is a tertiary aliphatic amine (TAA), which is naturally produced from the degradation of choline and carnitine—plant and mammal metabolites.[14] TMA can also be produced through industrial means (i.e., through human intervention) and exists in Earth's atmosphere as a pollutant from the methylation of NH_3 in the presence of a catalyst.[15–17] TMA is therefore only formed naturally through biotic means and stands as a potential biomarker in the search for extraterrestrial life.

Under UV photolysis, TMA is reported to dissociate into methyl and amine radical fragments.[18–22] While the detection of the methyl radical is hardly indicative of life, the detection of the amine radical fragment along with the detection of TMA in an extraplanetary atmosphere would strengthen the case for the presence of life. Thus, an understanding of the excited state processes at play within TMA and the nature of its photoproducts is vital in understanding the potential biological and chemical processes occurring on exoplanets and their atmospheres.

The deep UV-driven photochemistry of TAAs involves the initial excitation of a nitrogen lone pair electron to a manifold of Rydberg states.[23–27] This strong propensity for Rydberg states to undergo diagonal transitions ($\Delta v = 0$) to the cation state upon ionization results in narrow photoelectron bands and extreme sensitivity to changes in molecular geometry,[28] a characteristic that is exploited in Rydberg fingerprint spectroscopy measurements.[26,27,29,30] All of this is in contrast to valence state ionization, which tends to result in much broader, overlapping spectral features due to significant overlap with a wider range of vibrational states. This loss of resolution can limit our ability to map any changes in the energy of particular spectral features to subtle changes in molecular geometry.

In TMA, excitation at 200 nm leads to the population of the $3p_z$ Rydberg state. The $3p_z$ Rydberg state is coupled to a valence σ^* state via a conical intersection (CI). The CI is considered to be accessed by the elongation of a N–C bond after planarization of the molecule from its initial pyramidal structure.[27] This Rydberg–valence interaction is common to many amines and is analogous to that seen in ammonia, where it is the N–H bond that is extended.[23,26,31,32] Unlike ammonia, where the initial excited state is 3s in character, coupling of the $3p_z$ state to the lower-lying Rydberg states provides an alternative relaxation pathway in TMA. As such, two pathways exist as reported in previous time-resolved spectroscopic and scattering studies of TMA.[21,27] The following description details the overall picture concluded from both experiments. Initially, after excitation, the molecule planarizes. In this first observed pathway, the N–C bond extends, leading to the $3p_z/\sigma^*$ CI, the N–C bond breaks, and the formation of CH_3 is observed on a timescale of 540–640 fs. In the second pathway, internal conversion (IC) through the remaining $n = 3$ Rydberg manifold of states leads to the population of the 3s Rydberg state, fission of the N–C bond over a much longer timescale, and CH_3 formation on a 74 ps timescale.[21,27]

Nanosecond ion yield and imaging studies have also revealed a great deal of information regarding the photoproducts. The ion yield work of Forde *et al.* performed at a photolysis wavelength of 193 nm revealed that CH_3 was produced in tandem with either N-methylmethanimine (NMMA, $H_2C = NCH_3$) or dimethyl amidogen (DMA, CH_3NCH_3) with a branching ratio of 0.72:0.27.[19,20] More recent ion imaging studies by Onitsuka *et al.* only observed the production of CH_3 and DMA product pairs in their wavelength-dependent study (200–236 nm). The product pairs consisted of DMA $(\tilde{A}^2A_1)$ + CH_3 ($v_2 = 0$) and DMA $(\tilde{X}^2B_1)$ + CH_3 ($v_2 = 1$), where v_2 denotes the out of plane bending mode of CH_3. The excited $(\tilde{A}^2A_1)$ state of DMA lies ~1.6 eV above the ground $(\tilde{X}^2B_1)$ state and was therefore energetically accessible across the pump wavelengths studied. The level of vibrational excitation observed in the methyl fragment was concluded to be independent of the photolysis wavelength. This further suggested that the specific vibrational states populated in the excitation step had a limited impact on the outcome and that the level of vibrational excitation in the product was dependent on the shape of the electronic potential energy surface. Finally, while not a time-resolved experiment, the formation of excited and ground state DMA products was assigned to the previously identified slow and fast timescales of dissociation, respectively, given by a dual ring nature of the CH_3 product scattering images.[22] From this, TMA is considered to share similar dissociation dynamics to that of its close cousin—ammonia.[31,32]

While there is some common agreement between studies with regard to the lifetimes of the excited states and observation of products, the following question remains: what controls the branching between the dissociation pathways, and how can the large difference in appearance times be explained? Modern advances in time-resolved photoelectron spectroscopy allow us to directly observe all excited states and processes and give a more detailed picture of how these states and processes lead to a variety of photoproducts.[33–36] In this work, we utilize a universal, extreme ultraviolet (XUV) probe to monitor the time-dependent changes in the photoelectron spectrum of TMA. The measurements allow us to monitor structural and electronic state changes occurring in the Rydberg states and how these couple to the exit channels associated with the dissociation products within a single, unified experiment. The analysis of the experimental measurements is supported by quantum chemical calculations that provide further mechanistic details on the photolysis of TMA.

II. METHODOLOGIES

A. Experimental

Time-resolved photoelectron spectroscopy measurements were performed using Artemis at the Central Laser Facility. An in-depth experimental setup is given elsewhere,[37] with only a brief overview given below.

Pump and probe pulses were generated from the output of an amplified Ti:sapphire system (Red Dragon, KM Labs) operating at a central wavelength of 800 nm at 1 kHz repetition rate. The output was split, providing separately compressed pulses used to generate the pump and probe. The 200 nm pump was generated via second harmonic generation followed by two sum-frequency generation steps (800 + 400, and 266 + 800 nm) in a series of beta-barium borate crystals. This resulted in ~3 μJ of 200 nm. XUV probe pulses were generated via high harmonic generation (HHG) in an Ar gas jet. The HHG process was driven by the second harmonic (400 nm) of the fundamental, with a time-preserving monochromator subsequently used to select the 7th harmonic of the driver (21.6 eV, 57.4 nm). The isolated harmonic has a nominal flux of 10^{10} photons per second on the target.[38] The minimum energy resolution afforded by the probe was taken from a Gaussian fit of the signals present in the photoelectron spectrum of Xe, presented in the supplementary material, and yielded 75 meV at photoelectron kinetic energies of ~8 eV. Pump and probe pulses were independently propagated, focused, and overlapped at a small angle (~3°) at the interaction point of the electron time-of-flight spectrometer and the molecular beam. The resulting pump–probe cross-correlation, obtained from our fitted instrument response function, yielded a Gaussian duration, (σ), of 82 fs.

The molecular beam was generated by expanding ~1 bar of 2% trimethylamine in helium (BOC specialty gases) through the 200 μm nozzle of a piezoelectric valve (Amsterdam Cantilever) operating at a 1 KHz repetition rate. The resultant molecular beam was skimmed once before entering the detection chamber. The liberated photoelectrons were detected using an electron time-of-flight spectrometer (Kaesdorf ETF11). Experiments were performed under two different detector settings where the entrance lens voltage was set to maximize the collection efficiency of high energy photoelectrons originating from ionization of the excited Rydberg states population (lens voltage of 110 V) or much lower energy electrons associated with the dissociation products (lens voltage of 80 V). All other settings were kept consistent between measurements.

B. Theory

All extended multi-state complete active space with second-order perturbation theory (XMS-CASPT2)[39,40] calculations were performed using the BAGEL 1.1 program package.[41,42] An imaginary shift of 0.2 au was employed with a single-state single-reference treatment of the multi-state component. In the orbital-optimization procedure, all 1*s*-core orbitals (non-hydrogen atoms) were frozen. All calculations use either the 6-31++G(d)[43,44] or aug-cc-pVDZ[45–47] basis sets. In the XMS-CASPT2 calculations, the aug-cc-pVDZ density-fitted auxiliary basis was used. All minimum-energy arrangements and conical intersections were computed at the XMS-CASPT2 level of theory, where an active space containing four electrons and seven orbitals was selected and averaged across the six lowest singlet states. Additionally, numerical Hessian computations confirmed the nature of the minimum energy arrangements as true minima.

Equation-of-motion coupled cluster with singles and doubles (EOM-CCSD)[48–51] calculations and perturbative equation-of-motion multi-reference coupled cluster (MR-EOMPT)[52–56] calculations were run with the Orca 6.0.0 program suite.[57–61]

The active space used in the geometry-optimization procedures consists of the lone-pair orbital (n) of the nitrogen atom, the 3s and 3p$_{x,y,z}$ Rydberg orbitals, and finally, the σ and σ^* pair for one of the N–C bonds (see Fig. S6). At the S_0, S_1, and S_4 geometries, the σ/σ^* pair is highly localized across the N–C bond, and S_5 is a high-energy transition from σ to 3s. At the conical intersections (CIs), the dissociative σ^* state is among the six predicted roots. The excitation energies and potential energy surfaces explored herein use a slightly modified four-electron seven-orbital active space to help produce continuous surfaces (see Fig. 7), where a 3*d* orbital is included for small N–C distances, which then rotates out for σ^* as the bond elongates because the latter is very high in energy around the FC region.

III. RESULTS

In Fig. 1, we plot photoelectron spectra obtained at different pump–probe delays. The ground state spectrum is plotted in black and represents the pre-time zero background, which was subtracted from the overall data when looking at pump–probe signals. At early times after excitation, the excited state population is predominantly associated with the Rydberg states, leading to photoelectron signals at a binding energy of 2–4 eV. The spectrum recorded at a pump–probe delay of +2.4 ps is plotted in red. At much longer

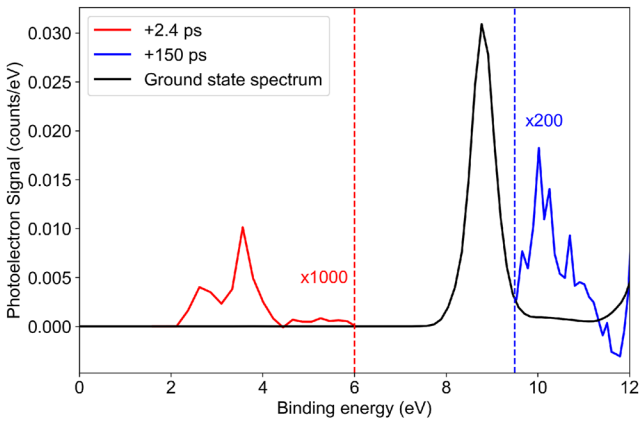

FIG. 1. Representative photoelectron spectra obtained at specific pump–probe delays with a 21.6 eV probe. The ground state photoelectron spectrum of TMA (black) is presented alongside the spectrum obtained from the excited molecule at a delay of +2.4 ps (red) as well as from the dissociation products at a delay of +150 ps (blue). The red and blue spectra are only plotted over the energy range of 0–6 and 9.5–12 eV, respectively. This removes regions of overlap where significantly different signal intensities and scaling factors are used and means that signals over the same energy region are not comparable. The intensity of the photoelectron signals associated with the Rydberg states and photoproducts has been scaled by ×1000 and ×200, respectively, to make them visible on the same scale as the ground state spectrum.

pump–probe delays, the photolysis reaction is complete, and signals associated with the formation of the photoproducts are expected at binding energies in the 9–12 eV range. A representative spectrum of the products recorded at our maximum pump–probe delay of +150 ps is plotted in blue. Note that due to the much lower signal intensity, the Rydberg and dissociation product signals have been multiplied by a factor of 1000 and 200, respectively, such that they can be plotted on the same intensity scale as the ground state spectrum.

A. Rydberg state dynamics

Concentrating on the early time dynamics, we present the time-resolved photoelectron spectrum of TMA over the energy region associated with the Rydberg states in Figs. 2 and 3. The data in Figs. 2 and 3 were collected with parallel and perpendicular polarizations of the pump and probe pulses, respectively. Note that we have presented the delay time axis in Fig. 2 on a linear scale up to +5 ps for direct comparison with Fig. 3. Due to the strong level of alignment induced by the initial excitation into the $3p_z$ Rydberg state, we expect the parallel and perpendicular polarizations to show different ionization propensities for the x, y, and z components of the 3p Rydberg manifold while alignment is maintained. In the parallel polarization data, the initial signal observed is centered at 2.6 eV and decays over a few picosecond timescale. The decay of the initial peak coincides with the appearance of a new peak at 3.5 eV, which appears to rise as a consequence of the decay of the first signal, indicating some IC processes between their respective states. The signal at 3.5 eV appears longer-lived and decays on a 100 ps timeframe. We assign the shorter-lived signal around 2.6 eV to the population of the 3p state and the longer-lived signal around 3.5 eV to the population of the 3s state. These assignments agree with those of Cardoza *et al.*[27] The 3s state signal decays over the next 70–100 ps and is consistent with previous measurements of the suspected decay of the 3s state.[21]

The data obtained with perpendicular pump and probe polarizations are plotted in Fig. 3. Due to the initial alignment of the molecule along the $3p_z$ axis upon excitation, the crossed pump–probe polarizations will lead to an enhanced ionization propensity of the $3p_{x,y}$ Rydberg states when compared with the parallel polarization measurements. The perpendicular polarization data show an initial onset of the signal at ~2.3 eV that shifts toward higher binding energies over the first 100 fs. Previous studies of TMA and similar TAAs have observed a similar shift associated with a planarization about the N atom.[21,23,26,27] We will discuss this feature in more detail in our discussion. After this initial shift, the signal then covers an energy range from 2.5 to 3.1 eV with a significant enhancement of the signal intensity at a binding energy around 3.0–3.1 eV when compared to the data obtained with parallel polarizations. This observation suggests that while the $3p_z$ and $3p_{x,y}$ components of our spectrum are heavily overlapped, the $3p_{x,y}$ signal is at a slightly higher binding energy and has a delayed appearance time when compared to the signal associated with the $3p_z$ state. As in the parallel polarization measurements, the 3s signal grows over the course of a few picoseconds and is observed at a binding energy of 3.5 eV. In both Figs. 2 and 3, it appears that the 3s Rydberg state signal may contain an oscillatory feature, in which the maximum intensity of the signal oscillates between the binding energies of 3.4 and 3.6 eV, respectively. This feature is more apparent at longer delay times (>10 ps) in Fig. 2 and at short delay times in

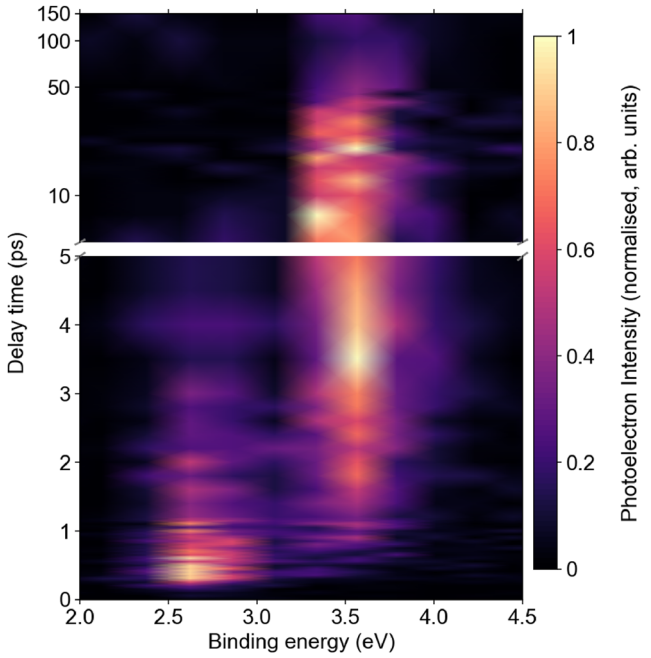

FIG. 2. Time-resolved photoelectron spectrum of TMA measured using parallel polarized pump and probe pulses. Note: the delay axis is on a mixed linear/logarithmic scale to highlight the changes in the Rydberg state signals.

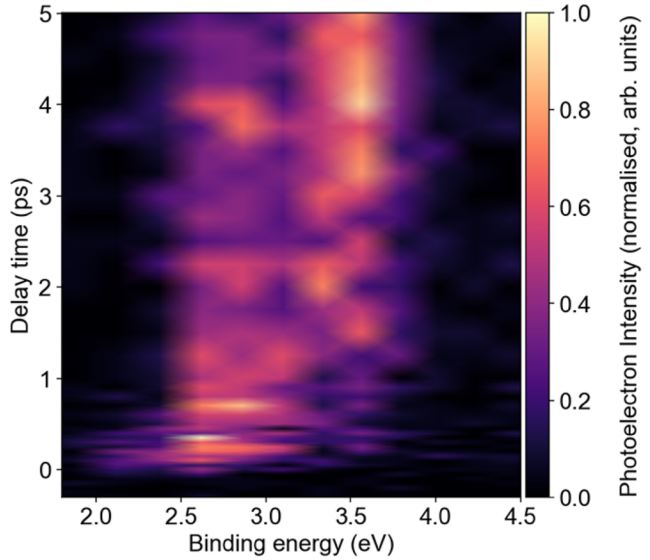

FIG. 3. Time-resolved photoelectron spectrum of TMA measured using perpendicularly polarized pump and probe pulses. Note we have plotted this over a slightly extended binding energy range (1.8–4.5 eV) to show the full extent of the initial shifting binding energy feature around 2–2.5 eV.

Fig. 3. While this feature may contain crucial dynamics information, we cannot ignore the possibility that this is at the limit of our signal to noise ratio in the photoelectron spectra. We, therefore, defer discussion of this feature to Sec. IV A.

To extract dynamic information pertaining to the Rydberg states, we performed a 2D global fit over the time-resolved photoelectron spectra shown in Figs. 2 and 3. Details of the global fitting procedure alongside analysis of the residuals are given in the supplementary material. Briefly, the global fit model is based on a Gaussian instrument response function, which is convolved with a series of exponential decay functions. The extracted decay-associated spectra (DAS) represent a specific spectral component with an associated exponential decay time constant. Within a specific DAS, regions of positive amplitude relate to exponential decays, while negative amplitudes relate to exponential rises occurring on the same timescale. Regions of positive and negative amplitude, therefore, allow us to map out the flow of population from one state to the other. The fit covers an extended binding energy range on either side of the spectrum (1.5–5 eV) to obtain a good baseline for each spectral component. To accurately recreate the full intensity map, we required a fit consisting of three DAS components.

We present the resultant DAS of the spectrum collected with parallel polarized pump and probe pulses (Fig. 2) in Figs. 4(a) and 4(b). The associated time constants are 400 ± 300 fs (4a), 4.4 ± 0.4 ps (4b, green), and 67 ± 14 ps (4b, maroon), respectively. In panel (a) we plot the initial signal observed in the spectrum centered at 2.6 eV with a tail that extends down to 2 eV, which has an associated time constant from the fit of 400 fs. We assign this peak to ionization from the initial $3p_z$ state. In panel (b), we plot two DAS associated with longer time constants. The DAS with the shorter time constant (green) has regions with positive and negative amplitudes. In the DAS with a 4.4 ps time constant, we observe positive amplitudes at binding energies below 3 eV and a negative component at around 3.5 eV. Based on the expected energies of the Rydberg states and in line with previous assignments, we assign the signal below 3 eV to the decay of the remaining 3p manifold of states, leading to the population of the 3s state seen at 3.5 eV. The final DAS component, with a time constant of 67 ps, represents and overlaps with the negative amplitude seen in the previous DAS. We, therefore, assign this to ionization from the 3s state whose population decays over a much longer timescale when compared to the 3p manifold of states.

To show the evolution of each spectral component more clearly, we plot integrated photoelectron intensities over binding energy ranges that are characteristic of the 3p (2.0–3.1 eV) and 3s (3.3–4.3 eV) states in Figs. 4(c) and 4(d), respectively. The data are plotted with 2σ uncertainties as error bars around each data point, with solid lines representing the fit obtained from the DAS over the same regions. In Fig. 4(c), we plot the integrated data and associated fit over the binding energy range of 2.0–3.1 eV. While we note that we cannot deconvolve the individual $3p_z$ and $3p_{x,y}$ fits from one another due to their heavy spectral overlap and lack of appropriate energy bins, in Fig. 4(c), the combined fit mimics the trend in the integrated data excellently. We also plot the resultant fit of the 3s state (red) and highlight the time-delayed rise in this state, which coincides with the decay of the 3p manifold. The time constants obtained from the fit are in agreement with previous time-resolved photoelectron spectroscopy studies made by Cardoza *et al.*, who obtained time constants of 540 fs and 2.9 ps for the

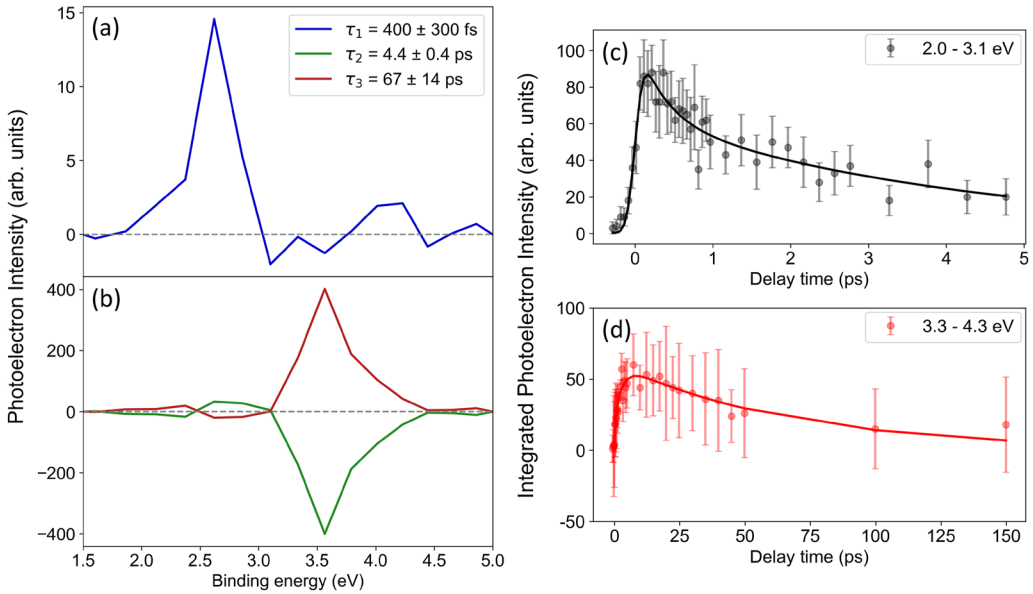

FIG. 4. DAS and resultant fits of the Rydberg states in Fig. 2. In (a) and (b), each spectral component is plotted with its associated timescales and 2σ errors given in the legend. In (c) and (d), fits of the integrated data based on the extracted time constants from the global fit are plotted with their respective errors (as bars). All errors (2σ values) were obtained by bootstrap analysis of the data. Further details are provided in Sec. IV of the supplementary material.

$3p_z$ and $3p_{x,y}$ respectively, and the time-resolved x-ray scattering experiments made by Ruddock *et al.*, who obtained a 3s lifetime of 74 ps.[21,27] The DAS obtained from a 2D global fit of the perpendicular polarization data is presented in Sec. V of the supplementary material and provides time constants within the experimental error of the time constants presented here. We note, however, that the spectral component associated with the initially populated $3p_z$ state is clearer within the binding energy range of 2.0–2.5 eV, which suggests that planarization is occurring within this state. This will be discussed further later.

B. Formation of the photoproducts

Having characterized the Rydberg state dynamics, we now turn to the formation of photoproducts. In Fig. 5, we plot the 9–12 eV binding energy range of the average background-subtracted photoelectron spectrum obtained at delays of 3–7 ps (red) and 50–150 ps (black) alongside the pre-time-zero baseline in gray (dashed). The delay ranges were selected to differentiate between products formed on the lifetimes of the 3p and 3s states, respectively. In the spectrum obtained between 3 and 7 ps, we see signals appear at energies between 10.3 and 11.2 eV, which then remain approximately constant out to the maximum delay measured. In the spectrum obtained between 50 and 150 ps, new signals between 9.6 and 10.3 eV are seen, indicating product formation over the longer timeframe. To visualize how these signals evolve, we have generated intensity profiles by integrating over the binding energy range of the signal as a function of pump–probe delay time, and these are plotted in Fig. 6. Due to the large difference in appearance time for the various fragments, we have plotted the delay time axis on a linear scale until 1 ps and on a logarithmic scale beyond. The boundary between scales is marked by the vertical gray dashed line.

Previous measurements have indicated that the dominant products channels are associated with the dissociation of one N–CH_3 bond and the formation of a ground state methyl radical (CH3) and DMA in either its ground ($\tilde{X}^2B_1$) or first electronically excited ($\tilde{A}^2A_1$) state.[19–22] The literature values for the ionization potential of CH_3, DMA($\tilde{X}^2B_1$), and DMA($\tilde{A}^2A_1$) are 9.84,[62] 9.01,[63] and 8.05 eV, respectively.[22] This means that while the CH_3 signal should appear in a relatively clear region of the photoelectron spectrum, the signal associated with ionization of ground and excited state DMA into the ground cation state would be obscured by their overlap with the TMA ground state background. Ionization into higher lying cation states for DMA ($\tilde{X}^2B_1$) would appear at around 9.65, 11.25, and 13.4 eV[63] and for DMA ($\tilde{A}^2A_1$) (based on an X–A energy gap of ~1.6 eV[22]) at 9.65 and 11.8 eV.[22] The values provided for the excited cation states relate to the maximum intensity of very broad peaks in the photoelectron spectrum, so they should be taken as a guide for what might be expected.

Comparing these expected values with those observed experimentally in Fig. 5 and their temporal profiles seen in Fig. 6, we see peaks around 9.6 and 10 eV that rise over tens of picoseconds to a maximum. There are other peaks at 10.4 eV and around 11 eV that show a rise over the course of the first picosecond. The 10 and

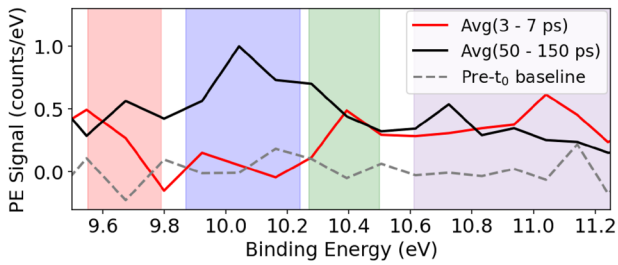

FIG. 5. Characteristic background subtracted and delay-averaged photoelectron spectra of the photolysis products of TMA. The delay-time-averaged spectrum obtained between 3 and 7 ps (red) and between 50 and 150 ps (black) is plotted alongside the pre-time-zero baseline (gray dashed) to visualize our spectral noise floor. The intensities in this spectrum have been normalized by the maximum signal obtained over all delays in this region. The shaded regions represent the regions integrated in the plots presented in Fig. 6.

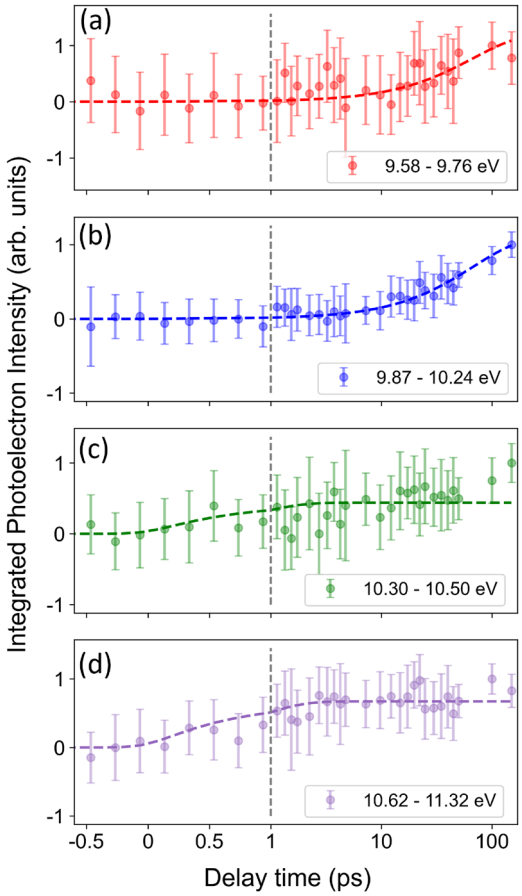

FIG. 6. Integrated photoelectron intensity as a function of time over the (a) 9.58–9.76 eV, (b) 9.87–10.24 eV, (c) 10.30–10.50 eV, and (d) 10.62–11.32 eV energy ranges. The error bars represent the 2σ confidence regions of the measurement obtained via bootstrapping. Due to the differences in rise times observed between products, we plot the full delay time range in the main figure on a linear scale until 1 ps and on a logarithmic scale beyond. The boundary between scales is marked by the vertical gray dashed line. Dashed lines are kinetic fits to the photoelectron intensity as discussed further in the main text alongside our assignments.

9.6 eV ranges match what one would expect for the formation of vibrationally cold CH_3 in conjunction with DMA. We cannot differentiate if this is electronically excited or ground state DMA due to their spectral overlap, but previous ion yield measurements suggest that the formation of DMA in the $(\tilde{A}^2A_1)$ state is the dominant dissociation channel.[22] We, therefore, assign the regions 9.55–9.79 and 9.87–10.24 eV to the formation of DMA $(\tilde{A}^2A_1)$ and CH_3 $(v = 0)$, respectively.

The two other product signals at 10.4 and 11.0 eV rise to their intensity maximum within the first few picoseconds after excitation. These peaks are a less obvious match to the expected products when only considering ionization into the electronic ground state of the cation. We, therefore, only provide speculative assignments here. Given the rapid formation time, we assume that these products are also associated with CH_3 and DMA fragments but in different quantum states. The 11 eV region closely matches the signals associated with the ionization of ground state DMA $(\tilde{X}^2B_1)$ into the first electronically excited cation state ($DMA^{+1}B_1$), while the 9.4 eV feature lies ~2400 cm^{-1} higher in energy than that associated with our main CH_3 signal, indicating significant vibrational excitation.[62] We, therefore, assign the faster rising peaks at 10.4 and 11 eV to the formation of vibrationally excited CH_3 in conjunction with ground state DMA.

To understand which excited states lead to the observed photoproducts, we have modeled the expected appearance times of the products based on the lifetimes extracted from the global fit of the Rydberg excited state signals. The models are based on a sequential kinetic model where the final product state has an infinite lifetime. The three possible pathways considered are therefore

$$\mathrm{TMA} \xrightarrow{h\nu} 3p_z \xrightarrow{k_{p_z}} \text{Products}, \tag{1}$$

$$\mathrm{TMA} \xrightarrow{h\nu} 3p_z \xrightarrow{k_{p_z}} 3p_{x,y} \xrightarrow{k_{p_{x,y}}} \text{Products}, \tag{2}$$

$$\mathrm{TMA} \xrightarrow{h\nu} 3p_z \xrightarrow{k_{p_z}} 3p_{x,y} \xrightarrow{k_{p_{x,y}}} 3s \xrightarrow{k_s} \text{Products}, \tag{3}$$

with decay constants, as obtained from the Rydberg state global fit of 2.74, 0.2257, and 0.0149 ps^{-1} for the $3p_z$, $3p_{x,y}$, and 3s states, respectively. Based on the known parameters, we can fit amplitudes to the product signal to see if any are consistent with the observed signals. Further details are given in supplementary material with the results of the fits plotted as dashed lines in Fig. 6.

The fits suggest that the fast rising products, which we have assigned as DMA $(\tilde{X}^2B_1)$ and vibrationally hot CH_3, appear on a timescale that is consistent with pathway 1, with the formation of products occurring directly from the decay of the $3p_z$ Rydberg state population, Figs. 6(c) and 6(d), while the DMA $(\tilde{A}^2A_1)$ and CH_3 $(v = 0)$ products, which appear to form over a much longer timeframe, are well-fitted to pathway 3, suggesting that product formation occurs from the 3s Rydberg state, shown in Figs. 6(a) and 6(b). The global view of the dynamics, therefore, supports the previous conclusions of Ruddock *et al.*,[21] who have previously suggested that there are competing IC/dissociation pathways in the $3p_z$ state. An overview of our assignments is given in Table I.

The experimental observations lead to the following dynamic picture. Initial excitation populates the $3p_z$ Rydberg state. Competing IC and dissociation processes lead to the majority of the population internally converting to the $3p_{x,y}$ states, while a minority of the population dissociates to form vibrationally hot CH_3 and DMA $(\tilde{X}^2B_1)$. The lifetime of the $3p_z$ state due to these processes is ~400 fs. The population of the $3p_{x,y}$ state stabilizes against further dissociation, and the only relaxation pathway is via IC into the 3s Rydberg state with a lifetime of ~4.4 ps. Decay of the 3s Rydberg state leads to dissociation of the N–C bond and formation of CH_3 and DMA $(\tilde{A}^2A_1)$ fragments with a 3s state lifetime of 67 ps.

TABLE I. Assignments of the product signals observed in Fig. 5. I_{max} is the binding energy of the maximum signal intensity. I_{range} is the binding energy range defining the overall signal.

I_{max} (eV)	I_{range} (eV)	Product assignment
9.7	9.58–9.76	DMA $(\tilde{A}^2A_1)$
10.0	9.87–10.24	CH_3 $(v = 0)$
10.4	10.30–10.50	Vibrationally hot CH_3
10.7	10.62–11.32	DMA $(\tilde{X}^2B_1)$

C. Computational results

To support our experimental assignments, we have performed a series of electronic-structure calculations. At the Franck–Condon (FC) region, where the ground state is dominated by a single configuration, the experimental excitation energies of the 3s and $3p_z$ states are well reproduced using EOM-CCSD/aug-cc-pVDZ (see Table II). The degenerate $3p_x/3p_y$ pair is found to be slightly lower in energy than the bright $3p_z$ state. The more expensive MR-EOMPT(4e,7o) level of theory delivers excitation energies within 0.1–0.2 eV of the experiment, even while using the nearly minimal, but appropriate, four-electron and seven-orbital active space.

At the ground state equilibrium, TMA favors a pyramidal arrangement with a central CCCN-dihedral angle (ϑ) and equivalent C–N distances (R) of 32.9° and 1.45 Å, respectively. However, for the Rydberg states, a near-planar arrangement, $\vartheta \sim 0°$, is favored. The optimal 3s and $3p_z$ geometries are very similar, with only a small difference in the methyl rotation, and both have an R of 1.45 Å. The ϑ and R at various critical points are provided in Table S3. The potential energy surface corresponding to a linear interpolation between the S_0 and 3s minima is shown in Fig. S6, where the parallel nature of the Rydberg states is clearly observed, which is in line with previous calculations.[64] The vertical binding energies (VBEs) of the Rydberg states at the minimum-energy geometries are provided in Table S4 using the EOM-CCSD level of theory, as this

TABLE II. Predicted 3s, $3p_x$, $3p_y$, and $3p_z$ excitation energies (eV) and the energy gap ΔE between the 3s and $3p_z$ states at the S_0 minimum energy geometry using various electronic-structure methods. All calculations were performed at the XMS-CASPT2(4e,7o)/6-31++G(d) optimized geometry.

Theory	3s	$3p_{x/y}$	$3p_z$	ΔE
EOM-CCSD/aug-cc-pVDZ	5.46	6.20/6.20	6.24	0.78
MR-EOMPT(4e,7o)/aug-cc-pVDZ	5.33	6.07/6.07	6.10	0.77
Experiment[27]	5.46	···	6.23	0.77

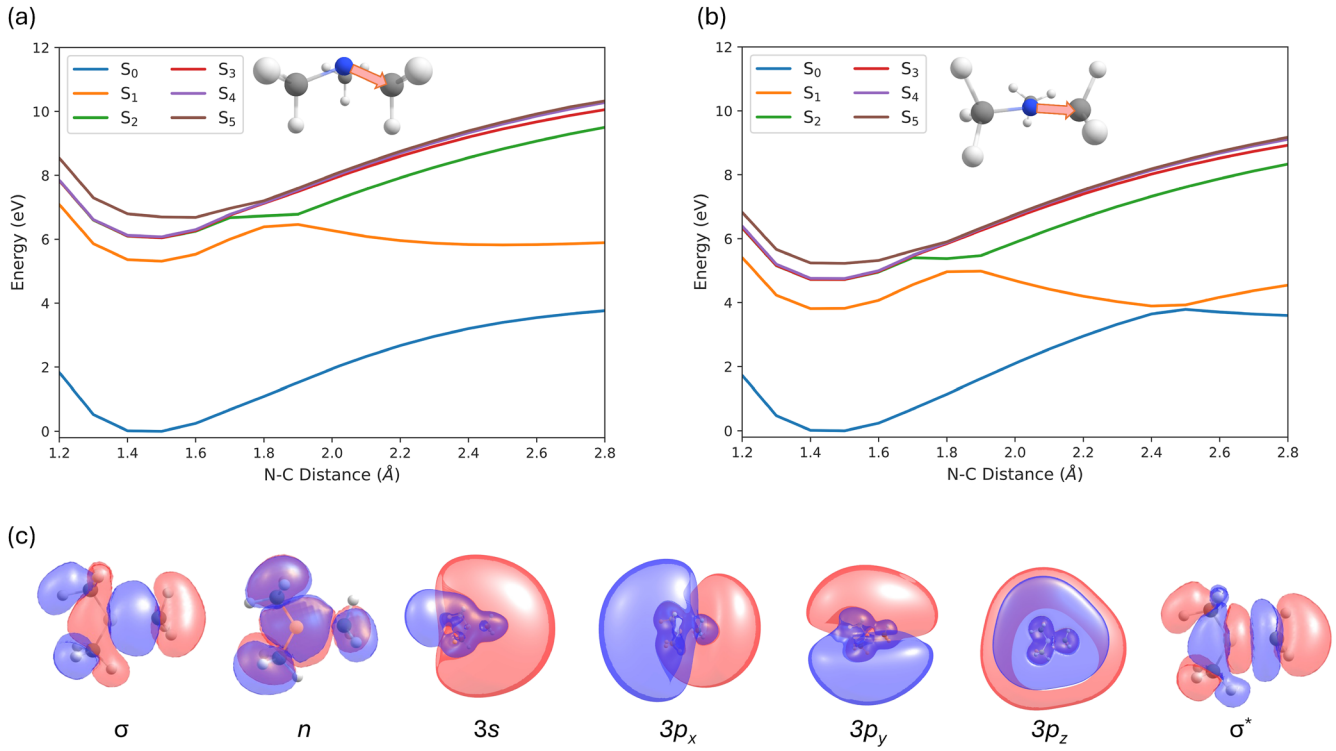

FIG. 7. MR-EOMPT(4e,7o)/aug-cc-pVDZ potential energy curves for methyl dissociation in both a pyramidal (a) and planar arrangement (b). The active space at an *R* of 1.9 Å has also been shown (c).

method has been shown to be remarkably accurate at FC geometries. The cation was modeled using unrestricted CCSD based on unrestricted Hartree–Fock orbitals. The vertical ionization energy (VIE) predicted using this approach is found to be in agreement with experiment, VIEs of 8.36 and 8.44 eV, respectively. For the 3s state, a small increase in the VBE of ~200 meV is predicted as the molecule planarizes, shifting from 2.91 to 3.08 eV. In contrast, the VBEs of the $3p_x$, $3p_y$, and $3p_z$ states are much less affected by this planarization. The predicted binding energies at the 3s and $3p_z$ minima are essentially unchanged for all the Rydberg states, highlighting the similarity between the minimum energy geometries, with only a small difference in the rotation of the methyl groups. In addition to the minimum energy arrangements, VBEs were also computed at a planar structure, which would be encountered if the pyramidal S_0 vibrational mode (ν_4 = 393.6 cm^{-1}) is populated. At this geometry, the 3s, $3p_x$, and $3p_y$ VBEs are similar to the other planar arrangements. However, the VBE of the $3p_z$ state is more sensitive to the location of the hydrogen atoms and is found to be lower by 70 meV, relative to S_0. Therefore, it is clear that due to the parallel nature of the potential energy surfaces, motion along this coupled planarization-methyl rotation coordinate is unlikely to drive IC, but in the case of the 3s state, a small shift in the photoelectron energy will be observed.

The excited state landscape for methyl dissociation was then explored. EOM-CCSD and single-reference methods, in general, are known to inadequately describe bond-breaking pathways as a result of the increase in multi-reference character as dissociation occurs. Therefore, the multi-reference method MR-EOMPT was used to investigate bond dissociation pathways, as it has been shown to yield accurate excitation energies, which are on par with EOM-CCSD (see Table II) and much more accurate than XMS-CASPT2(4e,7o), in the FC region. The adiabatic potential energy curves resulting from elongation of one N–C bond on XMS-CASPT2-optimized S_0 and 3s structures (pyramidal and planar, respectively) are pictured in Fig. 7.

At the FC region, the adiabatic states have the following diabatic representation: 3s (S_1), $3p_{x,y}$ ($S_{2,3}$), $3p_z$ (S_4), and 3d-type (S_5). The σ^* state is much higher in energy in the FC region, and as *R* increases, this state lowers in energy, and at ~1.7 Å, the 3d orbital rotates out of the active space in exchange for the σ^* orbital, leading to a change in character of S_5. In the discussion that follows, the diabatic representation is used. For both pyramidal and planar structures across the range of N–C bond distances considered, the 3s and 3p Rydberg states remain parallel to one another. The degeneracy between $3p_x$ and $3p_y$ lifts as *R* increases due to the alignment of one state along the bond-dissociating coordinate, introducing a degree of asymmetry. In the pyramidal dissociation surface, Fig. 7(a), the σ^* state cascades across the 3*p* manifold between 1.7 and 1.8 Å before crossing with the 3s state at around 1.9 Å. The σ^* state then runs parallel with S_0 and no crossing between the states is observed, leading adiabatically to the DMA ($\tilde{A}^2A_1$) + CH_3 dissociation products. For the planar geometries, Fig. 7(b), the excited state landscape

at N–C bond distances less than ~1.9 Å is virtually identical to that seen in the pyramidal structure. However, at more extended N–C bond distances, the energy of the σ^* state continues to lower until at a separation of 2.4 Å, and the σ^* state crosses, with S_0 thereby providing an IC pathway to ground state DMA $(\tilde{X}^2B_1)$ + CH_3 photoproducts.

IV. DISCUSSION

A. Dynamics of TMA photolysis

The combined experimental and theoretical investigation leads to the following model of the photolysis reactions of TMA. Upon absorption of light at 200 nm, the population is transferred into the $3p_z$ Rydberg state. Initial structural dynamics lead to a planarization of the initially pyramidal structure and a shift in the measured binding of approximately +0.3 eV. This is most clearly seen in the experimental measurements performed with perpendicular pump and probe polarizations, Fig. 3. This is a much broader shift in binding energy compared to the 100 meV reported by Cardoza *et al.*[27] In contrast, our calculated VBEs indicate a comparatively modest change (~20 meV). However, a significantly larger shift of ~90 meV relative to the $3p_z$ state minimum is obtained when the molecule is displaced along the ground state umbrella mode, corresponding to planarization about the central nitrogen atom, highlighting that the change in binding energy is particularly sensitive to geometric relaxation along this mode. While the theoretical results are broadly consistent with the trends observed by Cardoza *et al.* and those observed in this work, they do not fully reproduce the magnitude of the measured binding energy shift. This discrepancy may indicate limitations in the theoretical model's ability to fully capture the electronic response to such structural changes, or it may reflect the influence of experimental factors, such as spectral noise within the 2.0–2.5 eV region of Fig. 3 that could contribute to an enhanced apparent VBE shift.

Extension of one N–C bond leads to IC to the lower-lying components of the 3p and 3s manifold through coupling to the $\sigma^*_{(N-CH_3)}$ state, ultimately leading to the dissociation and formation of DMA $(\tilde{X}^2B_1)$ + vibrationally hot CH_3 reaction products on a subpicosecond timescale. The rigid scans presented in Fig. 7 confirm this excited state/dissociation channel and suggest that planarization, or the adoption of a near planar geometry (i.e., $\vartheta \sim 0$), must be a prerequisite for this channel. The minimum energy conical intersections were also computed (see Table S3). The $\sigma^*/3p_z$ CI and $\sigma^*/3s$ CI geometries were found to have a similar ϑ of ~8° and an R of 1.61 and 1.8 Å, respectively, while the σ^*/S_0 CI occurs at a near-planar geometry with an R of 2.45 Å. Therefore, a possible fast decay regime involves a coupled planarization and N–C bond stretch.

The vibrationally hot methyl fragment formed via the fast dissociation channel is seen to have an excess vibrational energy of ~2400 cm^{-1}. Previous measurements of TMA (and the secondary amine analogue dimethylamine) have shown that as the methyl group transitions from the pyramidal structure seen in the bound amines to the planar radical, there is excitation of the ν_2, umbrella mode of the CH_3 fragment.[22,65] The harmonic wavenumber of the umbrella mode in the methyl radical is equal to ~600 cm^{-1} such that the observed signal would correspond to ~4 quanta of the ν_2 mode. Alternative assignments based on combination bands could also be proposed, but, to the best of our knowledge, no other modes have been seen to be vibrationally excited in any previous measurements of TMA and could not be assigned here due to our limited energy resolution. We suggest that the initially excited population that undergoes rapid N–C stretching alongside planarization is most likely to lead to dissociation along this channel and gives rise to the high levels of vibrational excitation of the methyl fragment observed. We, therefore, tentatively assign the signal at 10.4 eV to the production of CH_3 ($\nu_2 = 4$) that is formed alongside the ground state DMA co-fragment.

The remaining 3p population internally converts to the 3s state with an associated time constant of 4.4 ps. Based on our rigid surfaces, upon reaching the $\sigma^*/3s$ CI, the population may instead undergo IC to the metastable 3s state, thus trapping the population. The 3s population is then observed to have a lifetime of ~67 ps that correlates with the formation of DMA $(\tilde{A}^2A_1)$ and CH_3 ($\nu = 0$). While there may be some evidence that the signals associated with the formation of vibrationally hot CH_3 and DMA $(\tilde{X}^2B_1)$ rise over this longer timescale, the change is small, suggesting that this, at most, is a very minor exit channel for population in the 3s state. The lack of vibrationally hot CH_3 and DMA $(\tilde{X}^2B_1)$ fragments over the longer timescale combined with the observation that the conical intersection leading to these is only accessible at planar geometries suggests that the exit channel from the metastable 3s structures goes through a non-planar structure that, therefore, avoids the conical intersection to the ground state. A barrier from the 3s minimum to $\sigma^*/3s$ CI of 1.15 eV is encountered in both the planar and pyramidal rigid scans. It should be noted that this is not an optimized barrier and, therefore, will likely be larger than that observed in reality. Additionally, the potential energy surface of the 3s state along the pyramidalization coordinate is considerably shallow, with planar and pyramidal geometries separated by 0.2 eV. This would lead to an increase in non-planar geometries, which would then dissociate to DMA $(\tilde{A}^2A_1)$ and CH_3 ($\nu = 0$) and be in competition with DMA $(\tilde{X}^2B_1)$ + vibrationally hot CH_3 dissociation, the latter being observed only at near-planar geometries. The 0.2 eV wide oscillatory feature observed in the 3s state photoelectron signal (Figs. 2 and 3) may be the direct spectroscopic evidence for the excited state population accessing planar and non-planar geometries due to the agreement between the observed and calculated binding energy differences. However, the expected period of oscillation, based on the computed vibrational frequency of the umbrella mode, is only 85 fs. Our measurement sampling rate means we do not map out the signal on an appropriate timescale to see such oscillation. We, therefore, cannot confidently assign this to anything molecular based on the current data. Therefore, while suggestive of this process, we can only tentatively suggest that this feature corresponds to the 3s population oscillating between planar and non-planar geometries.

Finally, we consider the nature of the driver for branching in the $3p_z$ state. Wavelength-dependent measurements by Onitsuka *et al.* showed that varying the excitation energy—and thus the vibrational energy in the initially populated $3p_z$ state—had no impact on the vibrational state of the CH_3 products. This rules out vibrational excitation as a driver of pathway selection and instead points toward the geometry and surface structure as the key controlling factors.[22] Our results, in agreement with previous work by Cardoza and Ruddock, show that excitation into the $3p_z$ state leads to planarization around

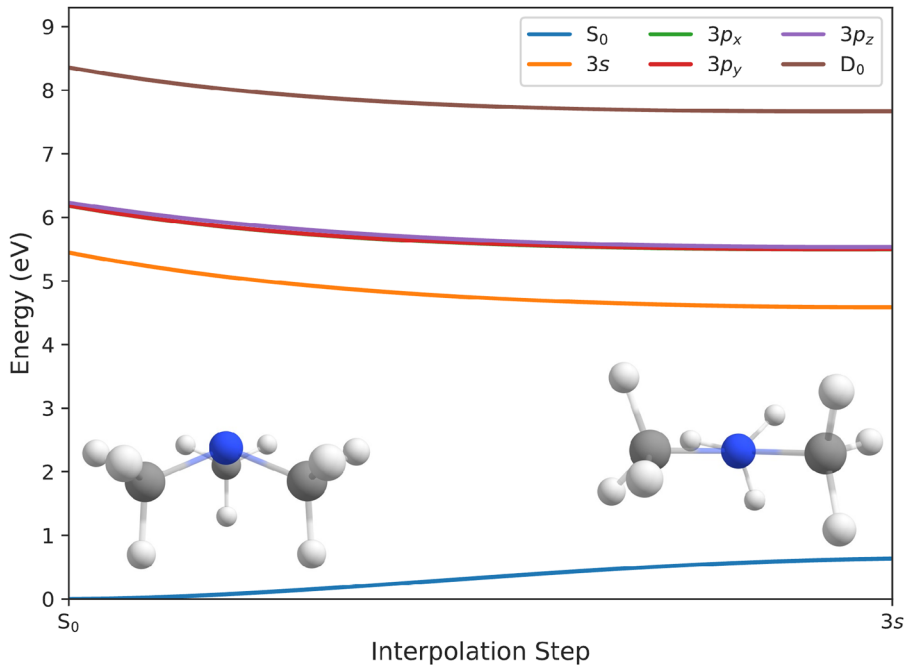

FIG. 8. (Unrestricted) (EOM-)CCSD/aug-cc-pVDZ predicted energies for the linear interpolation between the S_0 and 3s minimum energy arrangements. The S_0 and 3s minimum energy arrangements are shown at the lower left and right of the plot.

the nitrogen atom.[21,27] However, our computed planarization surfaces (Fig. 8) are shallow and offer no strong energetic incentive for planarization to occur. In fact, planarization would need to happen in tandem with N–CH_3 bond extension to access the fast dissociation pathway. While a planar geometry appears to be a prerequisite for direct dissociation via the fast channel, it is not required for IC to the lower Rydberg states, which leads to the slower pathway. This implies that branching is, at least partially, governed by the specific geometries adopted within the $3p_z$ state and whether they facilitate access to dissociative intersections or routes.

The integrated product signals in Fig. 6 show a higher yield for the slow-channel products—DMA $(\tilde{A}^2A_1)$ and CH_3 $(v = 0)$—indicating that the slow dissociation pathway is dominant, while the fast channel is a minor route. This aligns with Onitsuka's findings.[22] Taken together, these results suggest that the branching in the $3p_z$ state is ultimately controlled by the relative strengths of nonadiabatic couplings: between $3p_z$ and σ^* and between $3p_z$ and $3p_{x,y}$. The dominance of the slow pathway and the preference for DMA $(\tilde{A}^2A_1)$ and CH_3 $(v = 0)$ products imply that coupling between the latter is stronger, making internal conversion more favourable than direct dissociation under most geometries.

While we are unable to determine branching ratios between these two exit channels, future non-adiabatic molecular dynamics simulations will seek, in part, to determine this alongside calculations of the non-adiabatic coupling terms for each pathway (σ^* and $3p_{x,y}$) with the $3p_z$ state. Additional outstanding questions regarding the dynamics at play will also be addressed, including the geometries accessed during direct dissociation on the 3s state and the extent and contributions to energy partitioning in the products of both ground state and 3s state exit channels.

B. Implications as a biomarker

While our experimental and theoretical efforts have not revealed new spectroscopic information that would strengthen the case for TMA as a biomarker, we have revealed which spectral signature would confirm the presence of TMA in an extraplanetary atmosphere—that of DMA. From our experimental results, we have confirmed that the DMA moiety is produced in its ground and excited states. However, as the low-lying excited state of DMA is expected to be non-dissociative,[22] we would expect ground state recovery on a nanosecond timescale via fluorescence or via non-radiative means. Thus, the ultimate confirmation of TMA will be by the spectral signatures of DMA $(\tilde{X}^2B_1)$. We note, however, that the DMA moiety is also produced through the photodissociation of dimethylamine in the 200–220 nm pump regime.[65] Dimethylamine is a secondary aliphatic amine, which is only known to be produced through the methylation of ammonia with a catalyst at elevated temperatures and increased pressures abiotically or biotically through the decay of marine life.[66,67] Thus, we highlight that DMA $(\tilde{X}^2B_1)$ may also form from dimethylamine, which may also be considered a potential biomarker.

This proposal of TMA as a biomarker does have some caveats, like all biomarkers, which must be considered: (1) the traditional catalyst used in the production of TMA is alumina (Al_2O_3), which has been found in geological samples, such as Corundum around hydrothermal sites (volcanic and impact).[68] With the sheer high temperatures produced by these sites and the potential for ammonia and methanol to exist in another atmosphere as it does in Earth's atmosphere, the production of TMA may be possible, which may give rise to a false positive detection of life.[8,9,69] (2) Other atmospheric processes, such as photolysis of DMA or subsequent collisions with other gas-phase atmospheric species, may lower the

concentration of the DMA moiety below the limit of detection.[8,69,70] This problem is, however, a technological problem with our current telescopes, although next generation telescopes, such as the James Webb Space Telescope, aim to improve their sensitivities to these faint biomarker signals.[70] Finally, we note that although TMA appears to be an ideal candidate as a biomarker, the detection of TMA does not rule out the possibility of an abiotic synthetic origin confidently—much like the recent story of phosphine on Venus[71] and dimethyl sulphide on exoplanet K2-18b.[6] Further research into natural, abiotic synthetic origins will be required upon a confirmed detection of TMA in an extraplanetary atmosphere.

V. CONCLUSIONS

We have performed a combined experimental and theoretical study of the photolysis reactions of TMA. The use of an XUV probe allows us to follow the complete reaction path and, through correlation of excited state lifetimes and product formation times, helps define the reaction pathways. Absorption of 200 nm light by TMA leads to population of the $3p_z$ Rydberg state. N–C bond extension in conjunction with planarization of the excited state leads to rapid dissociation of some of the excited state population into vibrationally hot CH_3 ($\nu_2 = 4$) and DMA ($\tilde{X}^2B_1$) facilitated by the $3p_z/\sigma^*_{(N-CH_3)}$ CI within the first picosecond. The remaining bound population undergoes sequential IC processes through the Rydberg manifold, eventually leading to the 3s state ($3p_z \rightarrow 3p_{x,y} \rightarrow 3s$). The metastable 3s state has a lifetime of ~67 ps before dissociation where it adiabatically forms DMA ($\tilde{A}^2A_1$) and CH_3 ($v = 0$). We suggest that dissociation via the DMA ($\tilde{A}^2A_1$) product channel is facilitated by a non-planar geometry, in which TMA must pass through an energy barrier of 1.15 eV to access.

Finally, we have identified that the DMA ($\tilde{X}^2B_1$) would act as a confirmational spectral signature of a photolyzed TMA in an extraplanetary atmosphere, thus strengthening a positive detection of TMA (and possibly life) on an alien planet.

SUPPLEMENTARY MATERIAL

The supplementary material contains a description of data processing steps associated with resolution characterization, calibration, and global fit procedures alongside the background material for the computational section.

ACKNOWLEDGMENTS

All authors would like to thank the Science and Technology Facilities Council (STFC) for access to the Artemis facility and the Engineering and Physical Sciences Research Council (EPSRC) for access to the Cirrus high-performance computing system. D.J.H. would like to thank ELI Beamlines and the University of Southampton for a studentship. H.J.T. would like to thank the STFC XFEL hub for physical sciences and the University of Southampton for a studentship. R.S.M., A.K., and L.B. thank the EPSRC for financial support (Grant Nos. EP/X027635/1 and EP/X026698/1). R.T.C. thanks the EPSRC for financial support (Grant No. EP/X026981/1). M.J.P. acknowledges the EPSRC for funding through Grant Nos. EP/T021675 and EP/V006746. A.W.P., A.K., and M.J.P. acknowledge the Leverhulme Trust (Grant No. RPG-2020-208). A.K. further acknowledges EPSRC Grant Nos. EP/V006819/2, EP/V049240/2, and EP/X026973/1 and the U.S. Department of Energy, Office of Science, Basic Energy Sciences, under Award No. DE-SC0020276. We would like to thank Charles Cockell at the University of Edinburgh for fruitful discussions about the possibility and caveats surrounding trimethylamine as a potential biomarker. This work was supported by the Netherlands Organisation for Scientific Research (NWO) under Grant No. VIDI.193.037 and the European Regional Development Fund (EFRO, OP Oost) under Project No. PROJ-00949.

AUTHOR DECLARATIONS

Conflict of Interest

The authors have no conflicts to disclose.

Author Contributions

Derri J. Hughes: Data curation (equal); Formal analysis (equal); Visualization (equal); Writing – original draft (lead); Writing – review & editing (equal). **Andrew W. Prentice**: Formal analysis (equal); Visualization (equal); Writing – review & editing (equal). **Lauren Bertram**: Formal analysis (equal); Writing – review & editing (equal). **Richard T. Chapman**: Data curation (equal); Methodology (equal); Writing – review & editing (equal). **Luca Craciunescu**: Data curation (equal); Writing – review & editing (equal). **Daniel A. Horke**: Data curation (equal); Writing – review & editing (equal). **Peter Krüger**: Data curation (equal); Writing – review & editing (equal). **Michael A. Parkes**: Data curation (equal); Writing – review & editing (equal). **Henry J. Thompson**: Data curation (equal); Writing – review & editing (equal). **Emma Springate**: Project administration (equal); Resources (equal). **James O. F. Thompson**: Data curation (equal); Methodology (equal); Writing – review & editing (equal). **Yu Zhang**: Data curation (equal). **Adam Kirrander**: Data curation (equal); Project administration (equal); Software (equal); Supervision (equal); Writing – review & editing (equal). **Martin J. Paterson**: Data curation (equal); Project administration (equal); Software (equal); Supervision (equal); Writing – review & editing (equal). **Russell S. Minns**: Conceptualization (equal); Data curation (equal); Funding acquisition (equal); Methodology (equal); Project administration (equal); Supervision (equal); Writing – original draft (equal); Writing – review & editing (equal).

DATA AVAILABILITY

The data that support the findings of this study are available from the corresponding author upon reasonable request.

REFERENCES

[1] J. L. Birkby, "Spectroscopic direct detection of exoplanets," in *Handbook of Exoplanets*, edited by H. J. Deeg and J. A. Belmonte (Springer International Publishing, Cham, 2018), pp. 1485–1508.

[2] P. Patapis, E. Nasedkin, G. Cugno, A. M. Glauser, I. Argyriou, N. P. Whiteford, P. Mollière, A. Glasse, and S. P. Quanz, "Direct emission spectroscopy of exoplanets with the medium resolution imaging spectrometer on board JWST MIRI: I. Molecular mapping and sensitivity to instrumental effects," Astron. Astrophys. **658**, A72 (2022).

[3]T. Encrenaz, "Infrared spectroscopy of exoplanets: Observational constraints," Philos. Trans. R. Soc., A **372**, 20130083 (2014).
[4]A. Loeb and D. Maoz, "Detecting biomarkers in habitable-zone earths transiting white dwarfs," Mon. Not. R. Astron. Soc.: Lett. **432**, L11–L15 (2013).
[5]S. Seager, M. Schrenk, and W. Bains, "An astrophysical view of earth-based metabolic biosignature gases," Astrobiology **12**, 61–82 (2012).
[6]N. Madhusudhan, S. Sarkar, S. Constantinou, M. Holmberg, A. A. A. Piette, and J. I. Moses, "Carbon-bearing molecules in a possible Hycean atmosphere," Astrophys. J. Lett. **956**, L13 (2023).
[7]L. Kaltenegger and F. Selsis, "Characterizing habitable extrasolar planets using spectral fingerprints," C. R. Palevol **8**, 679–691 (2009), part of Special Issue: Traces de vie présente ou passé: quels indices, signatures ou marqueurs?.
[8]C. A. Batty, V. K. Pearson, K. Olsson-Francis, and G. Morgan, "Volatile organic compounds (VOCs) in terrestrial extreme environments: Implications for life detection beyond Earth," Nat. Prod. Rep. **42**, 93–112 (2025).
[9]N. W. Reed, R. L. Shearer, S. E. McGlynn, B. A. Wing, M. A. Tolbert, and E. C. Browne, "Abiotic production of dimethyl sulfide, carbonyl sulfide, and other organosulfur gases via photochemistry: Implications for biosignatures and metabolic potential," Astrophys. J. Lett. **973**, L38 (2024).
[10]A. G. Fairén, J. Gómez-Elvira, C. Briones, O. Prieto-Ballesteros, J. A. Rodríguez-Manfredi, R. López Heredero, T. Belenguer, A. G. Moral, M. Moreno-Paz, and V. Parro, "The complex molecules detector (CMOLD): A fluidic-based instrument suite to search for (bio)chemical complexity on mars and icy moons," Astrobiology **20**, 1076–1096 (2020).
[11]A. F. Davila and C. P. McKay, "Chance and necessity in biochemistry: Implications for the search for extraterrestrial biomarkers in earth-like environments," Astrobiology **14**, 534–540 (2014).
[12]L. E. Rodriguez, J. M. Weber, and L. M. Barge, "Evaluating pigments as a biosignature: Abiotic/prebiotic synthesis of pigments and pigment mimics in planetary environments," Astrobiology **24**, 767–782 (2024).
[13]C. Pozarycki, K. M. Seaton, E. C. Vincent, C. Novak Sanders, N. Nuñez, M. Castillo, E. Ingall, B. Klempay, A. Pontefract, L. A. Fisher, E. R. Paris, S. Buessecker, N. B. Alansson, C. E. Carr, P. T. Doran, J. S. Bowman, B. E. Schmidt, and A. M. Stockton, "Biosignature molecules accumulate and persist in evaporitic brines: Implications for planetary exploration," Astrobiology **24**, 795–812 (2024).
[14]S. Craciun and E. P. Balskus, "Microbial conversion of choline to trimethylamine requires a glycyl radical enzyme," Proc. Natl. Acad. Sci. U. S. A. **109**, 21307–21312 (2012).
[15]A. B. van Gysel and W. Musin, "Methylamines," in *Ullmann's Encyclopedia of Industrial Chemistry* (John Wiley and Sons, Ltd, 2000).
[16]R. Cai, R. Yin, X. Li, H.-B. Xie, D. Yang, V.-M. Kerminen, J. N. Smith, Y. Ma, J. Hao, J. Chen, M. Kulmala, J. Zheng, J. Jiang, and J. Elm, "Significant contributions of trimethylamine to sulfuric acid nucleation in polluted environments," npj Clim. Atmos. Sci. **6**, 75 (2023).
[17]P. J. Silva, M. E. Erupe, D. Price, J. Elias, Q. G. J. Malloy, Q. Li, B. Warren, and D. R. Cocker III, "Trimethylamine as precursor to secondary organic aerosol formation via nitrate radical reaction in the atmosphere," Environ. Sci. Technol. **42**, 4689–4696 (2008).
[18]M. Kawasaki, K. Kasatani, H. Sato, H. Shinohara, N. Nishi, and T. Ibuki, "Molecular beam photodissociation of trimethylamine," J. Chem. Phys. **77**, 258–262 (1982).
[19]N. R. Forde, M. L. Morton, S. L. Curry, S. J. Wrenn, and L. J. Butler, "Photodissociating trimethylamine at 193 nm to probe dynamics at a conical intersection and to calibrate detection efficiency of radical products," J. Chem. Phys. **111**, 4558–4568 (1999).
[20]N. R. Forde, L. J. Butler, B. Ruscic, O. Sorkhabi, F. Qi, and A. Suits, "Characterization of nitrogen-containing radical products from the photodissociation of trimethylamine using photoionization detection," J. Chem. Phys. **113**, 3088–3097 (2000).
[21]J. M. Ruddock, N. Zotev, B. Stankus, H. Yong, D. Bellshaw, S. Boutet, T. J. Lane, M. Liang, S. Carbajo, W. Du, A. Kirrander, M. Minitti, and P. M. Weber, "Simplicity beneath complexity: Counting molecular electrons reveals transients and kinetics of photodissociation reactions," Angew. Chem., Int. Ed. **58**, 6371–6375 (2019).
[22]Y. Onitsuka, Y. Kadowaki, A. Tamakubo, K. Yamasaki, and H. Kohguchi, "Energy dependence of photodissociation dynamics of trimethylamine over the S_2 and S_1 excited states," Chem. Phys. Lett. **716**, 28–34 (2019).
[23]J. O. F. Thompson, L. B. Klein, T. I. Sølling, M. J. Paterson, and D. Townsend, "The role of novel Rydberg-valence behaviour in the non-adiabatic dynamics of tertiary aliphatic amines," Chem. Sci. **7**, 1826–1839 (2016).
[24]L. B. Klein, T. J. Morsing, R. A. Livingstone, D. Townsend, and T. I. Sølling, "The effects of symmetry and rigidity on non-adiabatic dynamics in tertiary amines: A time-resolved photoelectron velocity-map imaging study of the cage-amine ABCO," Phys. Chem. Chem. Phys. **18**, 9715–9723 (2016).
[25]M. Minitti, J. Gosselin, T. Sølling, and P. Weber, "The ultrafast photofragmentation pathway of n, n- dimethylisopropylamine," in *Femtochemistry VII*, edited by A. W. Castleman and M. L. Kimble (Elsevier, Amsterdam, 2006), pp. 44–48.
[26]S. Deb, B. A. Bayes, M. P. Minitti, and P. M. Weber, "Structural dynamics in floppy systems: Ultrafast conformeric motions in Rydberg-excited triethylamine," J. Phys. Chem. A **115**, 1804–1809 (2011).
[27]J. D. Cardoza, F. M. Rudakov, and P. M. Weber, "Electronic spectroscopy and ultrafast energy relaxation pathways in the lowest Rydberg states of trimethylamine," J. Phys. Chem. A **112**, 10736–10743 (2008).
[28]E. Oks, *Advances in Physics of Rydberg Atoms and Molecules* (IOP Publishing, 2021), Vol. 2053–2563.
[29]J. L. Gosselin and P. M. Weber, "Rydberg fingerprint spectroscopy: A new spectroscopic tool with local and global structural sensitivity," J. Phys. Chem. A **109**, 4899–4904 (2005).
[30]M. P. Minitti, J. D. Cardoza, and P. M. Weber, "Rydberg fingerprint spectroscopy of hot molecules: Structural dispersion in flexible hydrocarbons," J. Phys. Chem. A **110**, 10212–10218 (2006).
[31]N. L. Evans, H. Yu, G. M. Roberts, V. G. Stavros, and S. Ullrich, "Observation of ultrafast NH_3 (Ã) state relaxation dynamics using a combination of time-resolved photoelectron spectroscopy and photoproduct detection," Phys. Chem. Chem. Phys. **14**, 10401–10409 (2012).
[32]A. D. Smith, H. M. Watts, E. Jager, D. A. Horke, E. Springate, O. Alexander, C. Cacho, R. T. Chapman, and R. S. Minns, "Resonant multiphoton ionisation probe of the photodissociation dynamics of ammonia," Phys. Chem. Chem. Phys. **18**, 28150–28156 (2016).
[33]A. von Conta, A. Tehlar, A. Schletter, Y. Arasaki, K. Takatsuka, and H. J. Wörner, "Conical-intersection dynamics and ground-state chemistry probed by extreme-ultraviolet time-resolved photoelectron spectroscopy," Nat. Commun. **9**, 3162 (2018).
[34]S. Adachi, M. Sato, and T. Suzuki, "Direct observation of ground-state product formation in a 1,3-cyclohexadiene ring-opening reaction," J. Phys. Chem. Lett. **6**, 343–346 (2015).
[35]E. M. Warne, A. D. Smith, D. A. Horke, E. Springate, A. J. H. Jones, C. Cacho, R. T. Chapman, and R. S. Minns, "Time resolved detection of the S(^{1}D) product of the UV induced dissociation of CS_2," J. Chem. Phys. **154**, 034302 (2021).
[36]G. L. Abma, M. A. Parkes, W. O. Razmus, Y. Zhang, A. S. Wyatt, E. Springate, R. T. Chapman, D. A. Horke, and R. S. Minns, "Direct observation of a roaming intermediate and its dynamics," J. Am. Chem. Soc. **146**, 12595–12600 (2024).
[37]A. D. Smith, E. M. Warne, D. Bellshaw, D. A. Horke, M. Tudorovskya, E. Springate, A. J. H. Jones, C. Cacho, R. T. Chapman, A. Kirrander, and R. S. Minns, "Mapping the complete reaction path of a complex photochemical reaction," Phys. Rev. Lett. **120**, 183003 (2018).
[38]F. Frassetto, C. Cacho, C. A. Froud, I. C. E. Turcu, P. Villoresi, W. A. Bryan, E. Springate, and L. Poletto, "Single-grating monochromator for extreme-ultraviolet ultrashort pulses," Opt. Express **19**, 19169–19181 (2011).
[39]T. Shiozaki, W. Győrffy, P. Celani, and H.-J. Werner, "Communication: Extended multi-state complete active space second-order perturbation theory: Energy and nuclear gradients," J. Chem. Phys. **135**, 081106 (2011).
[40]J. W. Park and T. Shiozaki, "Analytical derivative coupling for multistate CASPT2 theory," J. Chem. Theory Comput. **13**, 2561–2570 (2017).
[41]BAGEL: Brilliantly advanced general electronic-structure library, http://www.nubakery.org, under the GNU General Public License.
[42]T. Shiozaki, "Bagel: Brilliantly advanced general electronic-structure library," WIREs Comput. Mol. Sci. **8**, e1331 (2018).

[43]T. Clark, J. Chandrasekhar, G. W. Spitznagel, and P. V. R. Schleyer, "Efficient diffuse function-augmented basis sets for anion calculations. III. The 3-21+G basis set for first-row elements, Li–F," J. Comput. Chem. **4**, 294–301 (1983).
[44]R. Krishnan, J. S. Binkley, R. Seeger, and J. A. Pople, "Self-consistent molecular orbital methods. XX. A basis set for correlated wave functions," J. Chem. Phys. **72**, 650–654 (1980).
[45]T. H. Dunning, "Gaussian basis sets for use in correlated molecular calculations. I. The atoms boron through neon and hydrogen," J. Chem. Phys. **90**, 1007–1023 (1989).
[46]R. A. Kendall, T. H. Dunning, and R. J. Harrison, "Electron affinities of the first-row atoms revisited. Systematic basis sets and wave functions," J. Chem. Phys. **96**, 6796–6806 (1992).
[47]D. E. Woon and T. H. Dunning, "Gaussian basis sets for use in correlated molecular calculations. V. Core-valence basis sets for boron through neon," J. Chem. Phys. **103**, 4572–4585 (1995).
[48]D. J. Rowe, "Equations-of-motion method and the extended shell model," Rev. Mod. Phys. **40**, 153–166 (1968).
[49]J. Geertsen, M. Rittby, and R. J. Bartlett, "The equation-of-motion coupled-cluster method: Excitation energies of Be and CO," Chem. Phys. Lett. **164**, 57–62 (1989).
[50]J. F. Stanton and R. J. Bartlett, "The equation of motion coupled-cluster method. A systematic biorthogonal approach to molecular excitation energies, transition probabilities, and excited state properties," J. Chem. Phys. **98**, 7029–7039 (1993).
[51]A. K. Dutta, F. Neese, and R. Izsák, "Speeding up equation of motion coupled cluster theory with the chain of spheres approximation," J. Chem. Phys. **144**, 034102 (2016).
[52]M. Nooijen, O. Demel, D. Datta, L. Kong, K. R. Shamasundar, V. Lotrich, L. M. Huntington, and F. Neese, "Communication: Multireference equation of motion coupled cluster: A transform and diagonalize approach to electronic structure," J. Chem. Phys. **140**, 081102 (2014).
[53]M. H. Lechner, R. Iszak, M. Nooijen, and F. Neese, "A perturbative approach to multireference equation-of-motion coupled cluster," Mol. Phys. **119**, e1939185 (2021).
[54]M. Ugandi and M. Roemelt, "A recursive formulation of one-electron coupling coefficients for spin-adapted configuration interaction calculations featuring many unpaired electrons," Int. J. Quantum Chem. **123**, e27045 (2023).
[55]C. Kollmar, K. Sivalingam, B. Helmich-Paris, C. Angeli, and F. Neese, "A perturbation-based super-CI approach for the orbital optimization of a CASSCF wave function," J. Comput. Chem. **40**, 1463–1470 (2019).
[56]F. Neese, "Approximate second-order SCF convergence for spin unrestricted wavefunctions," Chem. Phys. Lett. **325**, 93–98 (2000).
[57]F. Neese, "Software update: The ORCA program system, version 4.0," WIREs Comput. Mol. Sci. **8**, e1327 (2018).
[58]F. Neese, "Software update: The ORCA program system—Version 5.0," WIREs Comput. Mol. Sci. **12**, e1606 (2022).
[59]F. Neese, "The orca program system," WIREs Comput. Mol. Sci. **2**, 73–78 (2012).
[60]F. Neese, F. Wennmohs, U. Becker, and C. Riplinger, "The ORCA quantum chemistry program package," J. Chem. Phys. **152**, L224108 (2020).
[61]F. Neese, "The SHARK integral generation and digestion system," J. Comput. Chem. **40**, 381 (2022).
[62]J. Dyke, N. Jonathan, E. Lee, and A. Morris, "Vacuum ultraviolet photoelectron spectroscopy of transient species. Part 7.—The methyl radical," J. Chem. Soc., Faraday Trans. **72**, 1385–1396 (1976).
[63]Q. Chunhua, H. Gongyi, and W. Dianxun, "The electronic structure of the $(CH_3)_2N$ radical and the pyrolysis mechanism of dimethylnitrosamine: A HeI photoelectron spectroscopic study," J. Phys. Chem. A **103**, 1972–1975 (1999).
[64]M. Pápai, X. Li, M. M. Nielsen, and K. B. Møller, "Trajectory surface-hopping photoinduced dynamics from Rydberg states of trimethylamine," Phys. Chem. Chem. Phys. **23**, 10964–10977 (2021).
[65]P. Wangchingchai, M. Karino, K. Yamasaki, and H. Kohguchi, "N–H and N–C bond dissociation pathways in ultraviolet photodissociation of dimethylamine," J. Phys. Chem. A **128**, 1871–1879 (2024).
[66]D. R. Corbin, S. Schwarz, and G. C. Sonnichsen, "Methylamines synthesis: A review," Catal. Today **37**, 71–102 (1997), part of Special Issue: Catalytic Amination Reactions.
[67]G. B. Neurath, M. Dünger, F. G. Pein, D. Ambrosius, and O. Schreiber, "Primary and secondary amines in the human environment," Food Cosmet. Toxicol. **15**, 275–282 (1977).
[68]S. Schmidt, A. Hertwig, K. Cionoiu, C. Schäfer, and A. K. Schmitt, "Petrologically controlled oxygen isotopic classification of cogenetic magmatic and metamorphic sapphire from Quaternary volcanic fields in the Eifel, Germany," Contrib. Mineral. Petrol. **179**, 55 (2024).
[69]C. Cockell, personal communication (2024).
[70]C. Impey, "Life beyond Earth: How will it first be detected?," Acta Astronaut. **197**, 387–398 (2022).
[71]J. S. Greaves, A. M. S. Richards, W. Bains, P. B. Rimmer, H. Sagawa, D. L. Clements, S. Seager, J. J. Petkowski, C. Sousa-Silva, S. Ranjan, E. Drabek-Maunder, H. J. Fraser, A. Cartwright, I. Mueller-Wodarg, Z. Zhan, P. Friberg, I. Coulson, E. Lee, and J. Hoge, "Phosphine gas in the cloud decks of Venus," Nat. Astron. **5**, 655–664 (2020).